

## Hydration of gadolinium oxide (GdO<sub>x</sub>) and its effect on voltage-induced Co oxidation in a Pt/Co/GdO<sub>x</sub>/Au heterostructure

Aik Jun Tan,<sup>1</sup> Mantao Huang,<sup>1</sup> Sara Sheffels,<sup>1</sup> Felix Büttner,<sup>1,2</sup> Sunho Kim,<sup>1</sup> Adrian H. Hunt,<sup>2</sup> Iradwikanari Waluyo,<sup>2</sup> Harry L. Tuller,<sup>1</sup> and Geoffrey S. D. Beach<sup>1</sup>

<sup>1</sup>Department of Materials Science and Engineering, Massachusetts Institute of Technology, Cambridge, Massachusetts 02139, USA

<sup>2</sup>National Synchrotron Light Source II, Brookhaven National Laboratory, Upton, New York 11973, USA



(Received 11 March 2019; revised manuscript received 5 May 2019; published 17 June 2019)

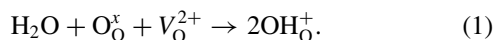
Magneto-ionic control of magnetism has garnered great interest in recent years due to the large magnetic changes that can be induced using a relatively small voltage. One model structure for this is Pt/Co/GdO<sub>x</sub>/Au, where Co is the magnetic layer and GdO<sub>x</sub> is the ionic conductor, with the magnetic properties dependent on the oxidation state of Co. While this structure is commonly used, there is limited understanding of the effect of GdO<sub>x</sub> properties on voltage-induced magnetic changes. In this work, we show that hydration of Gd<sub>2</sub>O<sub>3</sub> to form Gd(OH)<sub>3</sub> is crucial for voltage-induced Co oxidation in a Pt/Co/GdO<sub>x</sub>/Au device. By examining the rate of Co oxidation in nonhydrated and hydrated devices, we conclude that H<sub>2</sub>O in the GdO<sub>x</sub> layer acts as an oxidant during the voltage-induced Co oxidation process. Co oxidation through this interfacial reaction process is confirmed by *in situ* x-ray absorption spectroscopy.

DOI: [10.1103/PhysRevMaterials.3.064408](https://doi.org/10.1103/PhysRevMaterials.3.064408)

### I. INTRODUCTION

Electrical gating of magnetism has emerged as an important means to control spin-based devices. One promising route to effective gate voltage control is through voltage-induced ionic modulation of magnetic interfaces [1–13]. This method, dubbed magneto-ionics, has been used to achieve extremely large changes in properties such as magnetic anisotropy [1,3,4,6,7], magnetic moment [3,6,7,10,11,13], exchange bias [9], and spin-orbit torque [2,5] using a small gate voltage. In a majority of these devices, a Co/GdO<sub>x</sub> heterostructure is used [1–8,12,13], where Co is the magnetic layer, while GdO<sub>x</sub> acts as the ionic conductor. Although voltage-induced magnetic property changes in such structures have been widely studied, the ionic properties of GdO<sub>x</sub> and the detailed interfacial reactions are still not well understood.

Oxygen ion migration through the GdO<sub>x</sub> matrix has generally been assumed to be the operative mechanism in voltage-induced Co redox reactions in Co/GdO<sub>x</sub> stacks, but oxygen transport has not been directly observed and recent work suggests that moisture can play a critical role [4]. Many oxides readily absorb water from the atmosphere, incorporated as proton defects situated at oxygen ion vacancies through the following defect reaction [14]:



Here O<sub>O</sub><sup>x</sup> represents an oxygen ion on a normal oxygen site (denoted by the subscript O) where the superscript *x* is used by convention [14] to denote a net zero charge. V<sub>O</sub><sup>2+</sup> represents an oxygen vacancy with net double positive charge relative to the normally occupied lattice site, while OH<sub>O</sub><sup>+</sup> represents a proton defect comprising a singly positively charged proton localized around an oxygen ion sitting on a normal

oxygen site [15].<sup>1</sup> In proton conducting oxides, solid state dissolution of water molecules is an important process known to increase proton conductivity because the proton defects OH<sub>O</sub><sup>+</sup>, serve as “hopping” sites for proton conduction through the Grotthuss mechanism. It is also well established that humidity can alter the resistive switching behavior of oxides such as TaO<sub>x</sub> [16,17], HfO<sub>x</sub> [17], SiO<sub>x</sub> [18], and SrTiO<sub>x</sub> [19,20] in memristive cells due to its effect on bulk oxide properties and interface reactions at the anode and cathode. The high basicity of rare earth oxides makes them particularly hygroscopic [21], and they are known to react with moisture to form hydroxides [22–26] such as Gd(OH)<sub>3</sub> with consequent changes to electrical [25] and ionic properties [27].

Recent work has shown that in substrate/Co/GdO<sub>x</sub>/gate-electrode stacks, a positive gate voltage can electrochemically split atmospheric water and pump protons through the GdO<sub>x</sub>, to both reduce CoO to metallic Co and to modulate the magnetic anisotropy of a metallic Co thin film [4]. In this work, we show that water is equally important in the reverse process, namely oxidation of Co under negative gate bias. We demonstrate that H<sub>2</sub>O stored in GdO<sub>x</sub> as Gd(OH)<sub>3</sub> acts as the oxidant that oxidizes Co to CoO under negative gate bias, and that oxygen migration plays an insignificant role. We further show that hydrogen-induced CoO reduction leads to water uptake back into the GdO<sub>x</sub> matrix, allowing for closed-system electrochemical and magnetic property switching without the need for atmospheric exchange. These results provide a mechanistic understanding of magneto-ionic switching in metal/oxide heterostructures and essential insights to enable magneto-ionic device engineering.

<sup>1</sup>For those familiar with defect notation, V<sub>O</sub><sup>2+</sup> would also be written as V<sub>O</sub><sup>••</sup> and OH<sub>O</sub><sup>+</sup> as OH<sub>O</sub><sup>•</sup>.

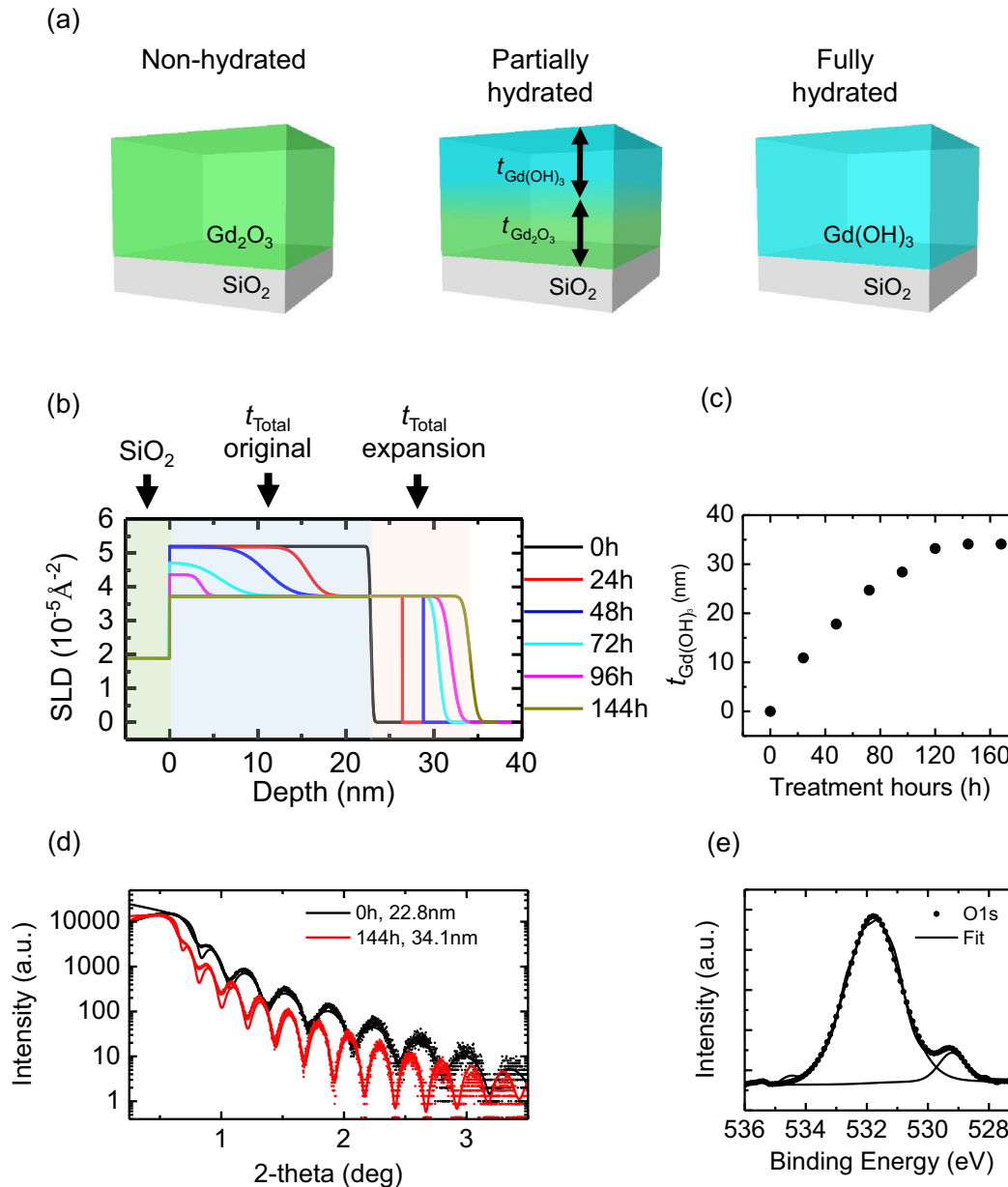


FIG. 1. (a) Schematic of a nonhydrated, partially hydrated, and fully hydrated  $\text{GdO}_x$  thin film on a  $\text{SiO}_2/\text{Si}$  substrate. (b) SLD of the  $\text{GdO}_x$  thin film as a function of hydration time. The fitted mass densities of  $\text{Gd}_2\text{O}_3$  and  $\text{Gd(OH)}_3$  are 8.3 and 6.0 g/cc, respectively. (c) Fitted thickness of  $\text{Gd(OH)}_3$  as a function of hydration time. (d) XRR spectra of a nonhydrated (0 h) and hydrated  $\text{GdO}_x$  thin film (144 h of hydration). The solid lines are the fitted models to the measured data (hollow circles). (e) XPS data of a 3-nm  $\text{GdO}_x$  thin film surface that has been exposed to ambient pressure for >2 weeks.

#### Probing water uptake through film expansion and chemical spectroscopy

Figure 1(a) shows the effect of hydrating a  $\text{GdO}_x$  thin film deposited on a  $\text{SiO}_2/\text{Si}$  substrate. The hydration treatment involves placing the sample at 90 °C under wet nitrogen gas at ambient pressure with  $P_{\text{H}_2\text{O}} = 525$  Torr, for up to 168 h. X-ray reflectivity (XRR) spectra were obtained periodically during the hydration process to follow the evolution of the film thickness and density. During hydration,  $\text{Gd}_2\text{O}_3$  is expected to react with  $\text{H}_2\text{O}$  to form  $\text{Gd(OH)}_3$  according to the reaction [24]:



The XRR spectra were fitted by modeling the film as a bilayer of  $\text{Gd}_2\text{O}_3$  and  $\text{Gd(OH)}_3$ , with variable thicknesses, roughnesses (structural and/or chemical), and mass densities [converted to x-ray scattering length densities (SLDs) in the fitting routine as described in the Supplemental Material II] [28]. Figure 1(b) shows SLD profiles corresponding to fits of the XRR spectra (Fig. S2), where two distinct layers are clearly resolved. With increasing hydration time, we observe a gradual progression of the  $\text{Gd(OH)}_3$  layer deeper into the film. The  $\text{GdO}_x$  film is a bilayer of dry  $\text{Gd}_2\text{O}_3$  at the bottom and a fully hydrated  $\text{Gd(OH)}_3$  at the top, with a diffuse interface in between. This diffuse interface arises from a gradient in

the water content, which is accounted for by a roughness (gradient) in the XRR fitting routine. Since the gradient is broad and the composition expected to be nonuniform, this intermediate region is not amenable to being fitted using an additional layer in the model. This gradient and its evolution with hydration can be seen between the two layers in the SLD profiles [Fig. 1(b)]. During the hydration process, the dry Gd<sub>2</sub>O<sub>3</sub> first dissolves water molecules in the form of proton defects according to Eq. (1). When the layer is completely hydrated, it forms Gd(OH)<sub>3</sub> according to net reaction depicted in Eq. (2). The transition region hence is expected to consist of a mixed phase of hydrated Gd<sub>2</sub>O<sub>3</sub> with dissolved water and Gd(OH)<sub>3</sub>.

Figure 1(c) shows the fitted thickness of the Gd(OH)<sub>3</sub> layer as a function of hydration time, while Fig. 1(d) shows the XRR spectra of the nonhydrated (0 h) and hydrated (144 h) GdO<sub>x</sub> films, respectively. From the data, we see that a 22.8-nm as-prepared GdO<sub>x</sub> film takes approximately 144 h to fully transform to Gd(OH)<sub>3</sub>. The fully transformed hydroxide shows an increase in thickness of 50%, expanding from 22.8 to 34.1 nm and a decrease in density of 28%, from 8.3 to 6.0 g/cm<sup>3</sup>. This corresponds very well to the transformation of monoclinic Gd<sub>2</sub>O<sub>3</sub> to Gd(OH)<sub>3</sub>, with bulk densities of 8.3 and 5.6 g/cm<sup>3</sup>, respectively [29,30].

In order to confirm the chemical state of the GdO<sub>x</sub> layer, we also performed x-ray photoelectron spectroscopy (XPS) on the surface of a 3-nm GdO<sub>x</sub> thin film which was exposed to ambient atmosphere for >2 weeks. Figure 1(e) shows the O1s spectrum of the thin film, where the data is best fitted by two peaks at 531.8 and 529.2 eV, which correspond to the O-H bond in Gd(OH)<sub>3</sub> and the O-O bond in Gd<sub>2</sub>O<sub>3</sub> [31,32], respectively. These results show that GdO<sub>x</sub> readily uptakes water even in ambient atmosphere to form a hydroxide phase.

## II. MAGNETIC CHARACTERIZATION

Figure 2 shows the comparison of voltage-induced Co oxidation between a nonhydrated and hydrated Pt (3 nm)/Co(0.9 nm)/GdO<sub>x</sub>(10 nm)/Au(3 nm) device. Here, we probe the magnetic state by measuring hysteresis loops probed locally using a polar magneto-optical Kerr effect (MOKE) polarimeter (Fig. S1). In its metallic state, the film exhibits a perpendicular magnetic anisotropy, whereas in the oxidized state there is no magnetic signal, which provides a convenient means to probe interfacial chemical state changes [4,6].

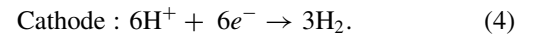
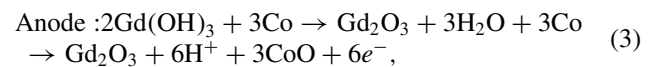
For the nonhydrated device, the top Au electrode was deposited using an *in situ* shadow mask immediately after the deposition of the Pt/Co/GdO<sub>x</sub> layers without vacuum break, so as to serve as a capping layer to minimize water uptake upon exposure to ambient atmosphere. Characterizations of the nonhydrated devices were then done immediately after fabrication (within a day) in order to preserve the nonhydrated state. For the hydrated device, the Pt/Co/GdO<sub>x</sub> structure was first placed at 90 °C under P<sub>H<sub>2</sub>O</sub> = 525 Torr for 72 h before the deposition of the top Au electrode. All gate voltages (V<sub>G</sub>) were applied to the top Au electrode, while the bottom Pt was grounded (see Methods).

Figure 2(a) shows a MOKE hysteresis loop of a virgin nonhydrated device while Figs. 2(b)–2(e) show MOKE hysteresis loops of the nonhydrated device after V<sub>G</sub> = −3 V has been

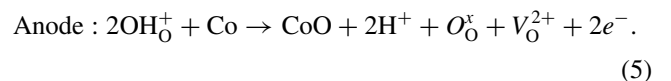
applied for 600 s in ambient, vacuum, wet N<sub>2</sub> and dry O<sub>2</sub> environments. The initially metallic Co in the virgin state is evidenced by a square out-of-plane MOKE hysteresis loop in Fig. 2(a). Under negative gate bias, no oxidation-induced magnetic property changes are observed [Figs. 2(b)–2(e)], even after 600 s in dry O<sub>2</sub> and wet N<sub>2</sub> for the nonhydrated device, indicating that oxygen migration and subsequent interfacial reactions are insignificant under these conditions.

Figures 2(f)–2(j) show the results of identical experiments for a device in which the GdO<sub>x</sub> has been fully hydrated. The out-of-plane MOKE hysteresis loop in the virgin state [Fig. 2(f)] shows that after hydration but before voltage application, Co remains metallic, indicating an absence of significant spontaneous oxidation during hydration (see Supplemental Material). This is consistent with the fact that hydrogen is more electropositive than Co and hence H<sub>2</sub>O should not spontaneously oxidize Co to CoO at room temperature without an applied potential.

Figures 2(g)–2(j) show that negative bias application results in complete loss in out-of-plane MOKE hysteresis, resulting from Co oxidation as observed elsewhere [6,7] and verified by x-ray absorption spectroscopy below. The fact that the Co layer is completely oxidized even in vacuum, indicates that (1) the oxidant is present in the GdO<sub>x</sub> layer, and (2) O<sub>2</sub> gas is not required for the oxidation process. These combined results can be explained using the schematic in Figs. 2(k)–2(j). When V<sub>G</sub> = −3 V is applied to the top Au gate of a nonhydrated device, the Co layer remains metallic due to the absence of any oxidant in the GdO<sub>x</sub> film. When V<sub>G</sub> = −3 V is applied to the top Au electrode of a hydrated device, H<sub>2</sub>O stored in the oxide film in the form of Gd(OH)<sub>3</sub> oxidizes Co to CoO [Eq. (3)]. The proton, H<sup>+</sup>, produced from the reaction is then driven by the electric field through the GdO<sub>x</sub> layer to the top Au electrode, where it is reduced by electrons, e<sup>−</sup> (flowing through the external circuit) to form hydrogen gas [Eq. (4)]. The net reactions, depicted in Fig. 2(l), are shown below:



The reaction described by Eq. (4) is also known as the hydrogen evolution reaction (HER) [33,34]. With Co and Gd(OH)<sub>3</sub> densities of 8.9 and 6.0 g/cc, respectively, the oxidation of 0.9 nm of Co would require the decomposition of only ~3 nm of Gd(OH)<sub>3</sub> (Supplemental Material IV). It is likely that Gd(OH)<sub>3</sub> does not completely transform to dry Gd<sub>2</sub>O<sub>3</sub> during the Co oxidation process. Rather, the Gd(OH)<sub>3</sub> should instead transform to a semihydrated GdO<sub>x</sub> with dissolved water, leading to a gradient in the water content adjacent to the Co interface. We note that the interface reaction corresponding to the case in which the GdO<sub>x</sub> adjacent to Co is not the fully transformed hydroxide phase but rather a hydrated oxide phase that would be described by



In this case, the cathode reaction will be the same as Eq. (3). This reaction could be controlling under conditions

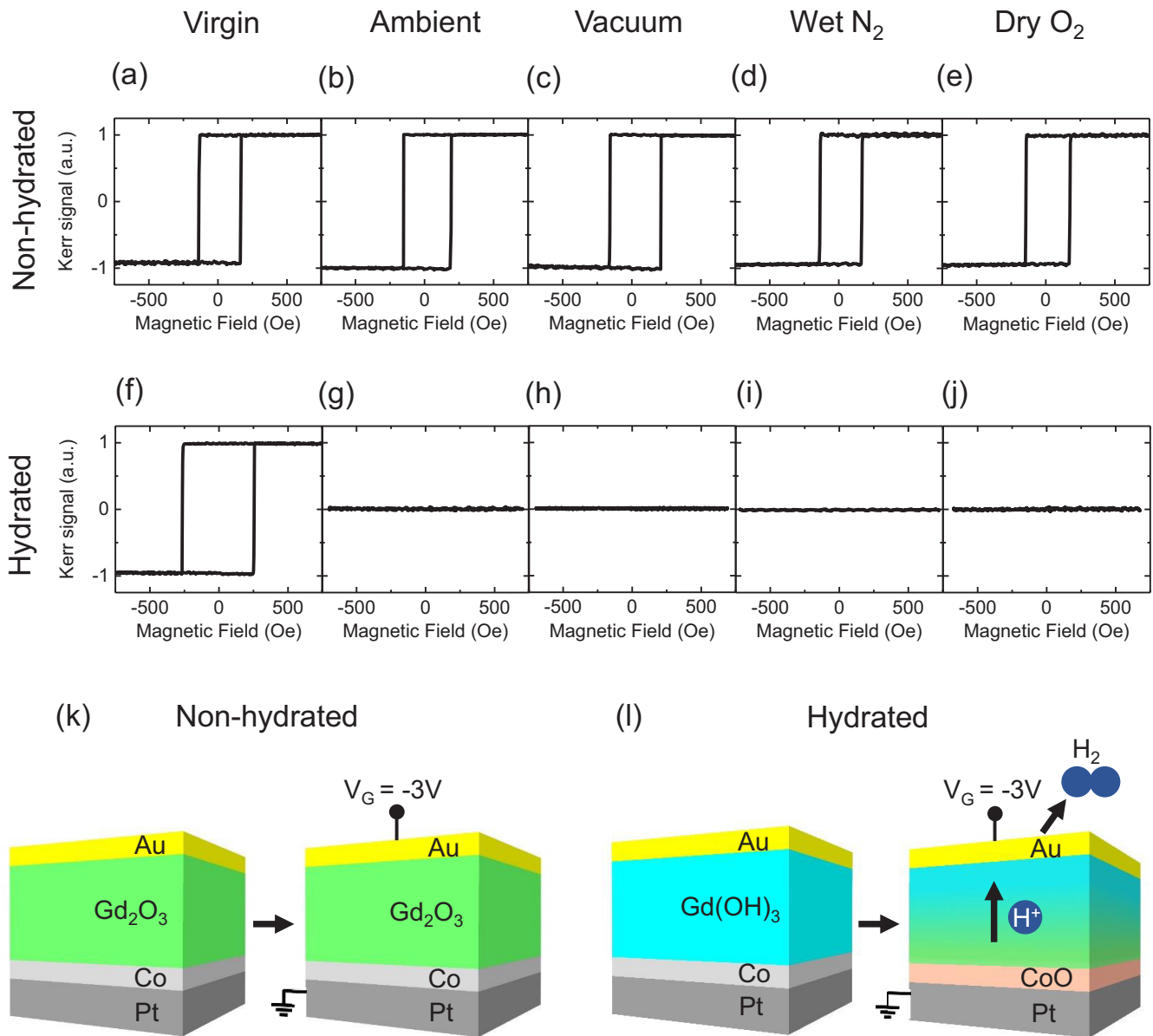


FIG. 2. (a)–(e) MOKE hysteresis loops of nonhydrated Pt(3 nm)/Co(0.9 nm)/GdO<sub>x</sub>(10 nm)/Au(3 nm) device in virgin state (a) and after  $V_G = -3$  V was applied for 600 s in ambient (b), vacuum (c), wet N<sub>2</sub> (d), and dry O<sub>2</sub> (e). (f)–(j) MOKE hysteresis loops of hydrated Pt(3 nm)/Co(0.9 nm)/GdO<sub>x</sub>(10 nm)/Au(3 nm) device in virgin state (f) and after  $V_G = -3$  V was applied for 600 s in ambient (g), vacuum (h), wet N<sub>2</sub> (i), and dry O<sub>2</sub> (j). (k)–(l) Schematic of voltage-induced reaction in a nonhydrated (k) and hydrated (l) device. The color gradient in the oxide layer in (l) represents a gradient in the incorporated water content.

where the cell is exposed to humid environments, but not as high as in this study where formation of hydroxide is observed. In both cases, the bottom Co acts as the anode, while the top Au acts as the cathode. The HER [33,34] at the top electrode is similar to the bottom-electrode reaction at positive gate bias in Ref. [12], where hydrogen insertion from atmospheric water splitting was used to modulate chemical and magnetic properties of the Co layer. Note that if oxygen were available at the cathode, the hydrogen formed at the cathode would react with the oxygen to form water as described previously in Ref. [12].

In order to further confirm the oxidation of Co by H<sub>2</sub>O in GdO<sub>x</sub>, we also fabricated thicker Au (15 nm) electrodes

on Pt/Co/GdO<sub>x</sub> to isolate the device from its surrounding atmosphere. Figure 3(a) shows the hysteresis loop of a virgin device with thicker Au electrode while Figs. 3(b)–3(c) shows the hysteresis loops after  $V_G = -3$  V has been applied for 600 s in ambient atmosphere and in vacuum, respectively. With thicker Au, we still observe complete oxidation of Co in roughly the same time as the thinner 3-nm Au device (Fig. S3). This further confirms that the oxidant is stored in the GdO<sub>x</sub> layer. Note that this is different from the case of CoO reduction in a Pt/CoO/GdO<sub>x</sub>/Au device, as studied in Ref. [12]. For this, the rate of reduction of CoO at  $V_G > 0$  depends crucially on the thickness of the top Au electrode because the reductant, H<sup>+</sup> is sourced from H<sub>2</sub>O in ambient atmosphere.

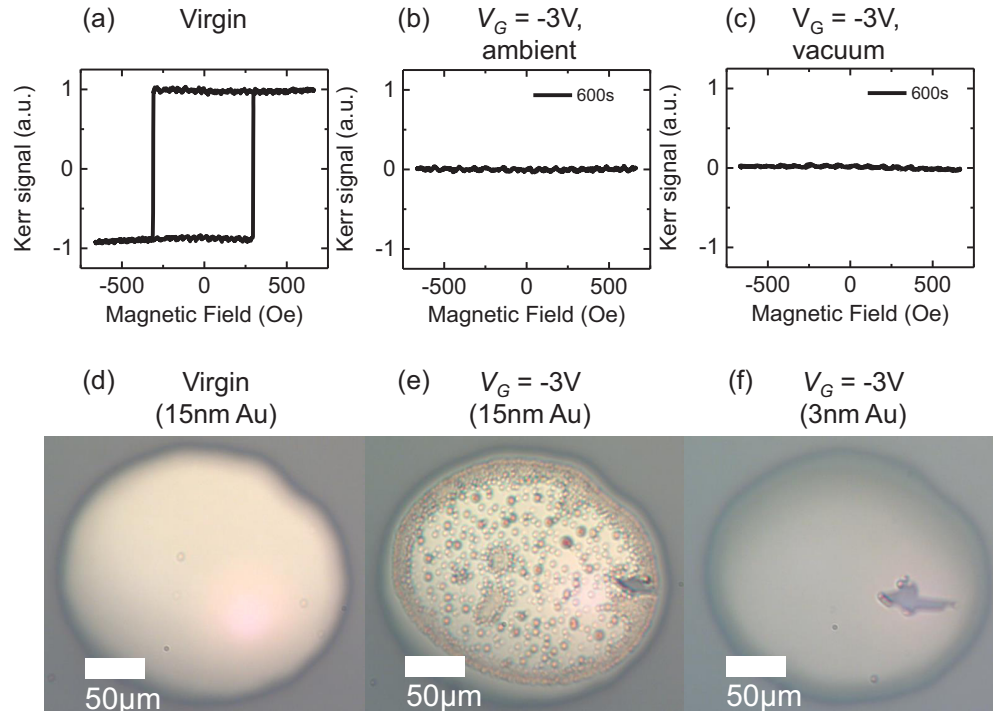


FIG. 3. (a)–(c) MOKE hysteresis loops of hydrated Pt(3 nm)/Co(0.9 nm)/GdO<sub>x</sub>(10 nm)/Au(15 nm) device in virgin state (a) and after  $V_G = -3$  V was applied for 600 s in ambient (b) and vacuum (c). (d), (e) Optical micrographs of Pt(3 nm)/Co(0.9 nm)/GdO<sub>x</sub>(10 nm)/Au (15 nm) devices before (d) and after (e) bias voltage application ( $V_G = -3$  V for 600 s) showing generation of hydrogen bubbles under the electrode. (f) Optical micrograph of Pt(3 nm)/Co(0.9 nm)/GdO<sub>x</sub>(10 nm)/Au (3 nm) after applying  $V_G = -3$  V for 600 s. The scratch marks on the side of the Au electrodes are due to the CuBe probes.

Figures 3(d)–3(e) show optical micrographs of a hydrated Pt(3 nm)/Co(0.9 nm)/GdO<sub>x</sub>(10 nm) device with 15-nm-thick Au top electrodes, before and after applying  $V_G = -3$  V for 600 s to completely oxidize the Co layer (see also Fig. S4). Circular protrusions of the electrode are clearly observed which indicates that gas bubbles are being formed leading to delamination. In order to verify if the gas bubbles are formed at the top GdO<sub>x</sub>/Au interface or bottom Co/GdO<sub>x</sub> interface, we also performed a similar experiment with a Pt(3 nm)/Co(0.9 nm)/GdO<sub>x</sub>(10 nm) device with 3-nm-thick Au after  $V_G = -3$  V is applied for 600 s [Fig. 3(f)]. In this case, no circular protrusions are observed because the electrode is porous and the evolved hydrogen gas escapes to the surrounding [6]. This indicates that the bubbles seen in the thicker Au electrode case are formed at the GdO<sub>x</sub>/Au interface, and this gas is necessarily H<sub>2</sub>, since the Au acts as the cathode at  $V_G = -3$  V. Because the features seen in Fig. 3(d) are permanent mechanical deformations, they remain upon applying a gate voltage of the opposite polarity. Note that gas bubble formation is also observed when  $V_G = -3$  V is applied for 600 s to Pt/Co/GdO<sub>x</sub>/Au devices in vacuum. This hydrogen evolution reaction was confirmed in our previous work [12] where Pd and Mg layers were inserted in a substrate/Mg/Pd/GdO<sub>x</sub>/Au stack structure and the formation of PdH<sub>x</sub> and MgH<sub>x</sub> was confirmed by XAS after applying a gate bias. In those experiments, a positive bias ( $V_G > 0$ ) was applied to the top Au electrode to insert hydrogen in the bottom Pd and Mg layers.

Interestingly, some of the hydrogen which is produced at the top Au electrode under  $V_G < 0$  can be stored in the cell. In order to demonstrate this, we compared the magnetoionic response of two Pt/Co(CoO)/GdO<sub>x</sub>/Au devices with a hydrated GdO<sub>x</sub> layer, where the Co layer has been oxidized. In the first device, the Co layer is metallic in its as-deposited state, and is then oxidized completely by first applying  $V_G = -3$  V for 300 s to the top 3nm Au [Fig. 4(a)]. In the second device, the Co layer is deposited in its oxidized state by reactive sputtering with oxygen gas [Fig. 4(d)]. A positive bias ( $V_G = +3$  V or +2V) bias is then applied to both devices in vacuum and in ambient atmosphere in order to reduce the CoO layer to metallic Co. This process has previously been shown to occur through injection of protons to the CoO layer, where they react with CoO to reduce it to a metallic state [4]. Figures 4(b) and 4(c) show the results for the first device in vacuum and ambient conditions respectively, while Fig. 4(e) and 4(f) show the corresponding results for the second device. For the first device, we can clearly see that some of the CoO is reduced in vacuum. This implies that some hydrogen is stored in the device after the initial  $V_G = -3$  V is applied that allows for closed-system electrochemical and magnetic property switching without the need for atmospheric exchange. The reduction of CoO to metallic Co by the stored hydrogen occurs through the reverse reactions described in Eqs. (3) and (4). In this case, at  $V_G > 0$ , the stored hydrogen donates its electrons driving the reduction of CoO to metallic Co.

On the other hand, for the second device where the Co layer is oxidized during deposition, we do not observe any

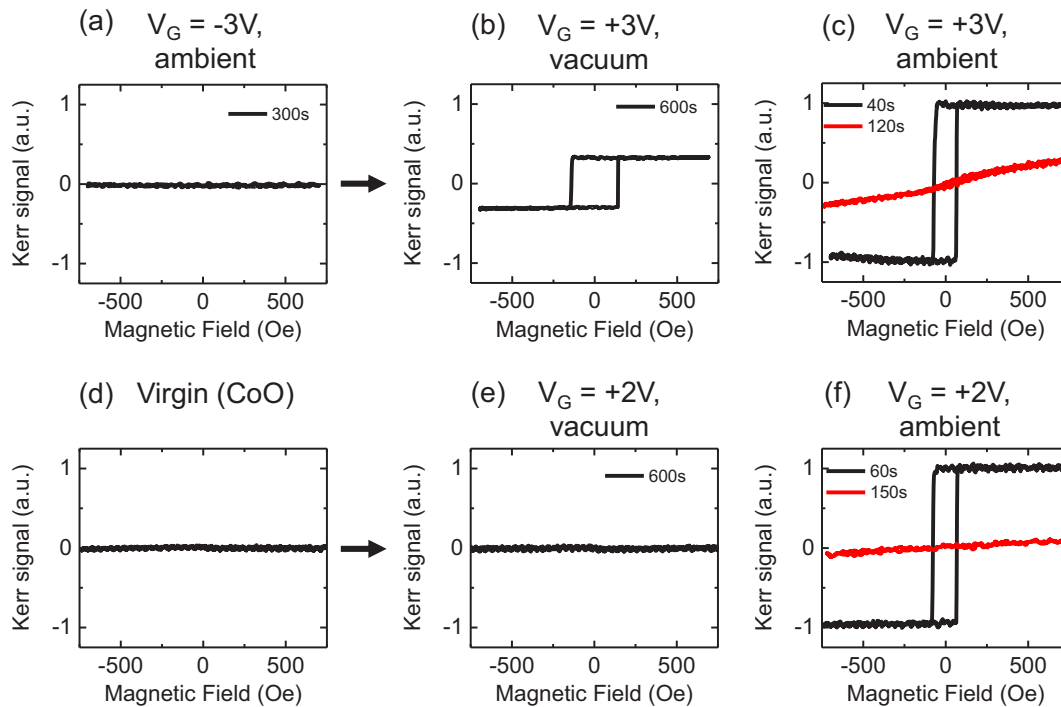


FIG. 4. (a) MOKE hysteresis loop of hydrated Pt(3 nm)/Co(0.9 nm)/GdO<sub>x</sub>(10 nm)/Au(3 nm) after  $V_G = -3$  V was first applied for 300 s in ambient to completely oxidize the metallic Co layer. (b), (c) MOKE hysteresis loops after  $V_G = +3$  V was applied to device in (a) under vacuum (b) and ambient (c) conditions in order to reduce the oxidized Co. (d) MOKE hysteresis loop of hydrated Pt(3 nm)/Co(0.9 nm)/GdO<sub>x</sub>(10 nm)/Au(3 nm) in virgin state. (e), (f) MOKE hysteresis loops after  $V_G = +2$  V was applied to device in (d) in vacuum (e) and in ambient atmosphere (f).

CoO reduction at  $V_G = +3$  V in vacuum [Fig. 4(e)]. The CoO layer is only reduced when the positive gate bias is applied in ambient, where humidity is present so that a water-splitting reaction can occur to provide a source of protons [Fig. 4(f)]. In both devices, a positive bias in ambient initially results in Co with perpendicular magnetic anisotropy. The Co magnetization then rotates in-plane as more hydrogen is accumulated near the Co layer [4]. The hydrogen can either accumulate at the Co/GdO<sub>x</sub> interface or diffuse through the Co layer to modify the Co/Pt interface. Previous studies have shown modulation of magnetic anisotropy in both cases [35,36]. Note that the observed anisotropy modulation is not due to delamination as it is completely reversible and the timescale for modulation is a few orders of magnitude shorter than the delamination process that occurs during bubble formation [4].

### III. CHEMICAL CHARACTERIZATION

To further verify the oxidation of Co through a direct chemical probe, we also performed *in situ* x-ray absorption spectroscopy (XAS) on a hydrated Pd(10 nm)/CoO(0.9 nm)/GdO<sub>x</sub>(30 nm)/Au(3 nm) device while applying gate biases under different atmospheric conditions. In this case, the hydration treatment at 90 °C and 525 Torr of P<sub>H2O</sub> is performed for only 24 h in order to retain a nonhydrated state at the CoO/GdO<sub>x</sub> interface. The first column of Fig. 5 show the XAS spectra around the Co  $L_2$ ,  $L_3$  edge [37,38], while the second column shows schematically the chemical state of the Co and the GdO<sub>x</sub> layers. In its virgin state, the Co layer is

initially oxidized [Fig. 5(a)], as seen from the Co  $L_3$  peak at  $\sim 780$  eV and  $L_2$  peak at  $\sim 795$  eV [13,37]. When  $V_G = +3$  V is applied to the top Au in vacuum, the CoO layer remains oxidized [Fig. 5(b)]; as a result, no changes in the  $L_3$  and  $L_2$  peaks are observed. When  $V_G = +3$  V is instead applied in 10 Torr of P<sub>H2O</sub>, the CoO layer is reduced to metallic Co by H<sup>+</sup> sourced from H<sub>2</sub>O [Fig. 5(c)] [4]. This is seen as a shift in the Co  $L_3$  peak from  $\sim 780$  to  $\sim 778$  eV, and a reduction in intensity of the Co  $L_2$  peak relative to  $L_3$  peak [13,37]. The H<sub>2</sub>O that is produced from this reaction is reincorporated back into GdO<sub>x</sub> in the form of Gd(OH)<sub>3</sub>. To confirm this, we next applied  $V_G = -3$  V to the metallic Co device in vacuum. The data show partial reoxidation of the metallic Co back to CoO, as evidenced by a broad peak at  $\sim 779$  eV. This peak comprises two Co  $L_3$  peaks at  $\sim 780$  and  $\sim 778$  eV, which indicates a mixture of CoO and Co. Similarly, if  $V_G = -3$  V is applied to the metallic Co in 10 Torr of P<sub>H2O</sub> instead of vacuum, partial reoxidation of the Co is also observed.

### IV. CONCLUSION

In conclusion, we have shown that a thin GdO<sub>x</sub> film expands by 50% in thickness upon hydration at relatively high humidity levels, consistent with the formation of a less dense Gd(OH)<sub>3</sub> film. This formation of Gd(OH)<sub>3</sub> is crucial for observation of voltage induced Co oxidation in a Pt/Co/GdO<sub>x</sub>/Au device. In particular, under a negative bias, it is the H<sub>2</sub>O derived from the decomposition of Gd(OH)<sub>3</sub> that oxidizes Co to CoO, rather than oxygen migration through the GdO<sub>x</sub> as has widely been assumed [6,7,9]. This reaction

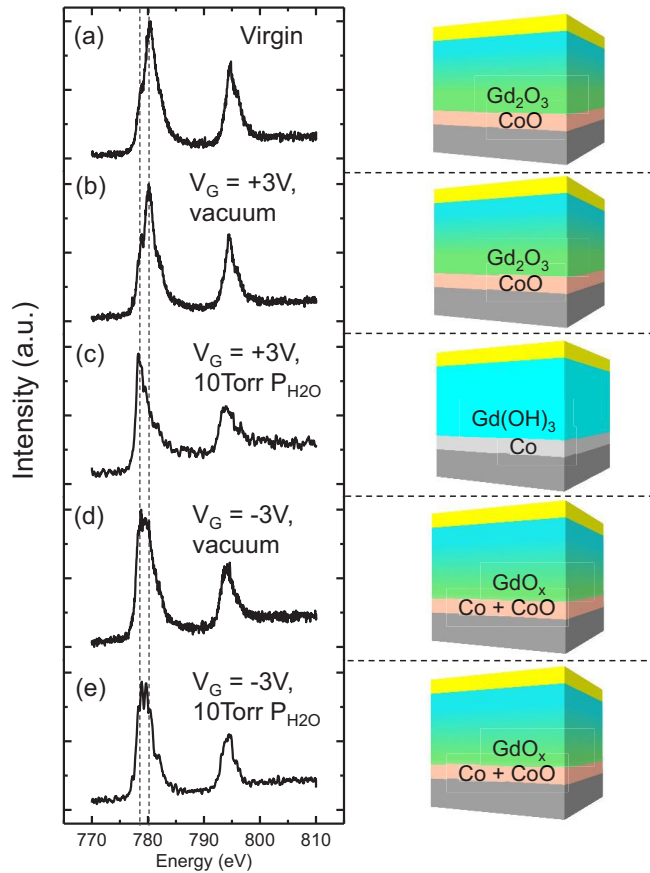


FIG. 5. (a)–(c) XAS spectra of Mg(30nm)/Pd(10 nm)/Co(0.9 nm)/GdO<sub>x</sub> (30 nm)/Au(3 nm) device in virgin state (a) and after  $V_G = +3$  V was applied for 600 s in vacuum (b) and in 10 Torr of P<sub>H2O</sub> (c), respectively. The experiments from (a) to (c) were done sequentially. (d), (e) XAS spectra of the device in (c) after  $V_G = -3$  V was applied for 600 s in vacuum and in 10 Torr of P<sub>H2O</sub>, respectively. Two different devices in (c) were used for experiments in (d) and (e).

produces H<sup>+</sup>, which is then driven by electric field towards the top Au to form hydrogen gas. We also demonstrated a closed-system electrochemical and magnetic property switching using the hydrogen and water storage property of GdO<sub>x</sub>.

## V. METHODS

**Sample preparation.** Ta(4 nm)/Pt(3 nm)/Co(0.9 nm)/GdO<sub>x</sub>( $t_{\text{GdO}_x}$  nm) films were fabricated on thermally oxidized Si (100) substrates using magnetron sputtering at room temperature and 3-mTorr Ar pressure. The metal layers were grown by DC sputtering. All GdO<sub>x</sub> layers were deposited using DC reactive sputtering with P<sub>O2</sub> of 0.07-mTorr except for the XAS samples, where the deposition was done using RF sputtering with P<sub>O2</sub> of 0.7 mTorr O<sub>2</sub>. For the samples described in Fig. 4 with Co in the initially oxidized state, the Co layer was reactively sputtered with P<sub>O2</sub> of 0.07-mTorr O<sub>2</sub> with a deposition time corresponding to the time required to deposit 0.9 nm of metallic Co. For MOKE measurements, 200- $\mu$ m diameter Au(3 nm) electrodes were patterned on top of the Ta/Pt/Co/GdO<sub>x</sub> continuous film, with the Ta (4 nm)/Pt(3 nm) underlayer uncovered by GdO<sub>x</sub> at the sample edge to

allow electrical contact to the back. For *in situ* XAS measurements, the Ta/Pt/Co/GdO<sub>x</sub>/Au structure was patterned into a cross-bar geometry with 1-mm arm width.

**X-ray reflectivity (XRR) measurements.** XRR was carried out using a Bruker D8 Discover HRXRD instrument with Cu K- $\alpha$  radiation at wavelength of 1.54 Å.

**X-ray photoelectron spectroscopy (XPS) measurements.** XPS was carried out using a Physical Electronics Versaprobe II x-ray photoelectron spectrometer at a base pressure of  $5 \times 10^{-9}$  Torr.

**Polar magneto-optical Kerr effect (MOKE) measurements.** MOKE measurements were performed using a 1 mW laser with a wavelength of 660 nm focused to spot size of  $\sim 10$   $\mu$ m. Experiments were performed in polar geometry and hence sensitive to the out-of-plane magnetization component. To apply gate voltage  $V_G$  to the circular electrodes, a CuBe probe was landed near the edge of the electrode and the Ta/Pt back electrode was grounded. The laser spot was focused at the middle of the electrode. All experiments were performed at room temperature. For experiments where different atmospheric conditions are required,  $V_G$  was applied ex-situ in a CPX-VF probe station. The MOKE hysteresis loop was measured before and after  $V_G$  was applied. Experiments under controlled gas environments were performed by backfilling the chamber with either O<sub>2</sub> gas (99.999% purity) or N<sub>2</sub> gas (99.999% purity). Humidity was introduced into the N<sub>2</sub> gas flow by bubbling through water. Wet N<sub>2</sub> and ambient atmosphere at 25 °C corresponds to  $\sim 20$  and 12 mT of H<sub>2</sub>O partial pressure, respectively. Vacuum condition corresponds to a base pressure of  $10^{-4}$  mbar. All experiments were performed at room temperature.

**X-Ray absorption spectroscopy (XAS).** *In situ* XAS data were taken at the *In situ* and Operando Soft X-ray Spectroscopy (IOS, 23-ID-2) beamline at the National Synchrotron Light Source II, Brookhaven National Laboratory. Partial fluorescence yield (PFY) spectra were acquired using a Vortex EM silicon drift detector. The incident soft x-ray beam has a footprint of  $\sim 100 \times 20$   $\mu$ m and is directed at 30° relative to the sample normal, while the PFY detector is positioned at 40° to the sample normal (Supplemental Material V). The sample used for the measurement has crossbar geometry with sample structure Ta (4 nm)/Mg(30 nm)/Pd(10 nm)/Co(0.9 nm)/GdO<sub>x</sub> (30 nm) and a 3-nm Au top gate. The XAS incident beam spot was located on the sample by first scanning the scanning stage to locate the crossbars through the total electron yield of the top Au electrode and chemical signature of the bottom electrode (Mg K edge) (More details in Supplemental Material V). Measurement is done with the  $V_G$  applied *in situ*. For experiments which require humidity, H<sub>2</sub>O vapor is introduced into the chamber through a leak valve and the flow rate is adjusted to maintain P<sub>H2O</sub> of 10 Torr. At vacuum condition, the main chamber pressure is  $\sim 2 \times 10^{-7}$  Torr after H<sub>2</sub>O evacuation, and the sample is kept at room temperature throughout the measurement.

## ACKNOWLEDGMENTS

This work was primarily supported by the National Science Foundation (NSF) through the Massachusetts Institute of Technology Materials Research Science and Engineering

Center (MRSEC) under Award No. DMR-1419807. The authors would also like to gratefully acknowledge C. Setten and L. Shaw for their assistance with the XRR and XPS measurements, respectively. This work made use of the Shared Experimental Facilities supported in part by the MRSEC Program of the National Science Foundation under

Award No. DMR-1419807. This research also used resources from the 23-ID-2 IOS beamline of the National Synchrotron Light Source II, a US Department of Energy (DOE) Office of Science User Facility operated for the DOE Office of Science by Brookhaven National Laboratory under Contract No. DE-SC0012704.

- 
- [1] U. Bauer, S. Emori, and G. S. D. Beach, *Nat. Nanotechnol.* **8**, 411 (2013).
- [2] S. Emori, U. Bauer, S. Woo, and G. S. D. Beach, *Appl. Phys. Lett.* **105**, 222401 (2014).
- [3] G. Hao, N. Noviaskey, S. Cao, I. Sabirianov, Y. Yin, C. C. Ilie, E. Kirianov, N. Sharma, A. Sokolov, A. Marshall, X. Xu, and P. A. Dowben, *J. Magn. Magn. Mater.* **451**, 487 (2018).
- [4] A. J. Tan, M. Huang, C. O. Avci, F. Büttner, M. Mann, W. Hu, C. Mazzoli, S. Wilkins, H. L. Tuller, and G. S. D. Beach, *Nat. Mater.* **18**, 35 (2019).
- [5] R. Mishra, F. Mahfouzi, D. Kumar, K. Cai, M. Chen, X. Qiu, N. Kioussis, and H. Yang, *Nat. Commun.* **10**, 248 (2019).
- [6] U. Bauer, L. Yao, A. J. Tan, P. Agrawal, S. Emori, H. L. Tuller, S. van Dijken, and G. S. D. Beach, *Nat. Mater.* **14**, 174 (2015).
- [7] C. Bi, Y. Liu, T. Newhouse-Illige, M. Xu, M. Rosales, J. W. Freeland, O. Mryasov, S. Zhang, S. G. E. Te Velthuis, and W. G. Wang, *Phys. Rev. Lett.* **113**, 267202 (2014).
- [8] D. A. Gilbert, A. J. Grutter, E. Arenholz, K. Liu, B. J. Kirby, J. A. Borchers, and B. B. Maranville, *Nat. Commun.* **7**, 12264 (2016).
- [9] D. A. Gilbert, J. Olamit, R. K. Dumas, B. J. Kirby, A. J. Grutter, B. B. Maranville, E. Arenholz, J. A. Borchers, and K. Liu, *Nat. Commun.* **7**, 11050 (2016).
- [10] S. Dasgupta, B. Das, Q. Li, D. Wang, T. T. Baby, S. Indris, M. Knapp, H. Ehrenberg, K. Fink, R. Kruk, and H. Hahn, *Adv. Funct. Mater.* **26**, 7507 (2016).
- [11] N. Lu, P. Zhang, Q. Zhang, R. Qiao, Q. He, H. B. Li, Y. Wang, J. Guo, D. Zhang, Z. Duan, Z. Li, M. Wang, S. Yang, M. Yan, E. Arenholz, S. Zhou, W. Yang, L. Gu, C. W. Nan, J. Wu, Y. Tokura, and P. Yu, *Nature (London)* **546**, 124 (2017).
- [12] T. Newhouse-Illege, Y. Liu, M. Xu, D. R. Hickey, A. Kundu, H. Almasi, C. Bi, X. Wang, H. Almasi, K. A. Mkhoyan, M. Xu, M. Rosales, Y. H. Xu, W. G. Wang, Y. Liu, J. W. Freeland, X. M. Cheng, C. J. Sun, D. J. Keavney, S. Zhang, T. Newhouse-Illige, D. Reifsnnyder Hickey, and A. Kundu, *Nat. Commun.* **8**, 15232 (2017).
- [13] M. Sakamaki and K. Amemiya, *Phys. Chem. Chem. Phys.* **20**, 20004 (2018).
- [14] T. Norby, M. Widerøe, R. Glöckner, and Y. Larring, *Dalt. Trans.* **0**, 3012 (2004).
- [15] H. L. Tuller and S. R. Bishop, *Annu. Rev. Mater. Res.* **41**, 369 (2011).
- [16] T. Tsuruoka, K. Terabe, T. Hasegawa, I. Valov, R. Waser, J. R. Jameson, K. Park, J. Lee, A. Nayak, Q. Wang, and Y. Itoh, *Jpn. J. Appl. Phys.* **55**, 06GJ09 (2016).
- [17] M. Lübben, S. Wiefels, R. Waser, and I. Valov, *Adv. Electron. Mater.* **4**, 1700458 (2018).
- [18] T. Tsuruoka, K. Terabe, T. Hasegawa, I. Valov, R. Waser, and M. Aono, *Adv. Funct. Mater.* **22**, 70 (2012).
- [19] F. Messerschmitt, M. Kubicek, and J. L. M. Rupp, *Adv. Funct. Mater.* **25**, 5117 (2015).
- [20] E. Sediva, W. J. Bowman, J. C. Gonzalez-Rosillo, and J. L. M. Rupp, *Adv. Electron. Mater.*, 1800566 (2018).
- [21] T. Moeller and H. E. Kremers, *Chem. Rev.* **37**, 97 (1945).
- [22] G. Adachi and N. Imanaka, *Chem. Rev.* **98**, 1479 (1998).
- [23] M. Fanciulli and G. Scarel, *Rare Earth Oxide Thin Films: Growth, Characterization and Applications* (Springer-Verlag, Berlin, Heidelberg, 2007).
- [24] S. Cohen, A. Abramovich, S. Zalkind, M. H. Mintz, I. Jacob, R. Akhvediani, M. Segev, A. Hoffman, and N. Shamir, *Surf. Sci.* **617**, 29 (2013).
- [25] S. Jeon and H. Hwang, *J. Appl. Phys.* **93**, 6393 (2003).
- [26] E. Külah, L. Marot, R. Steiner, A. Romanyuk, T. A. Jung, A. Wäckerlin, and E. Meyer, *Sci. Rep.* **7**, 43369 (2017).
- [27] Y. Larring and T. Norby, *Solid State Ionics* **77**, 147 (1995).
- [28] See Supplemental Material at <http://link.aps.org/supplemental/10.1103/PhysRevMaterials.3.064408> for a detailed description of the routine used to fit the x-ray reflectivity spectra.
- [29] P. Villars, *Gd<sub>2</sub>O<sub>3</sub> C-Phase Crystal Structure. Inorganic Solid Phases, SpringerMaterials (Online Database)* (Springer-Verlag, Berlin, 2016).
- [30] P. Villars, *Gd(OH)<sub>3</sub> Crystal Structure. Inorganic Solid Phases, SpringerMaterials (Online Database)* (Springer-Verlag, Berlin, 2016).
- [31] I. Aruna, B. R. Mehta, L. K. Malhotra, and S. M. Shivaprasad, *Adv. Funct. Mater.* **15**, 131 (2005).
- [32] C. R. Brundle and K. Wandelt, *Surf. Sci.* **157**, 162 (1985).
- [33] A. Lasia, in *Handbook of Fuel Cells—Fundamental Technology Applications* (John Wiley & Sons, Ltd., Chichester, 2003), pp. 417–434.
- [34] J. Tymoczko, F. Calle-Vallejo, W. Schuhmann, and A. S. Bandarenka, *Nat. Commun.* **7**, 10990 (2016).
- [35] B. Santos, S. Gallego, A. Mascaraque, K. F. McCarty, A. Quesada, A. T. N'Diaye, A. K. Schmid, and J. De La Figuera, *Phys. Rev. B* **85**, 134409 (2012).
- [36] S. M. Valvidares, J. Dorantes-Dávila, H. Isern, S. Ferrer, and G. M. Pastor, *Phys. Rev. B* **81**, 024415 (2010).
- [37] A. Manchon, C. Ducruet, L. Lombard, S. Auffret, B. Rodmacq, B. Dieny, S. Pizzini, J. Vogel, V. Uhlř, and G. Panaccione, *J. Appl. Phys.* **104**, 043914 (2008).
- [38] A. Manchon, S. Pizzini, J. Vogel, V. Uhlř, L. Lombard, C. Ducruet, S. Auffret, B. Rodmacq, B. Dieny, and G. Panaccione, *J. Appl. Phys.* **103**, 07A912 (2008).